

Article

# Computational Analysis of the Performance Characteristics of a Supercritical CO<sub>2</sub> Centrifugal Compressor

Senthil Kumar Raman  and Heuy Dong Kim \* 

Department of Mechanical Engineering, Andong National University, 1375 Gyeongdong-ro, Andong-si 36729, Gyeongsangbuk-do, Korea; skumar@anuis.andong.ac.kr

\* Correspondence: kimhd@andong.ac.kr

Received: 16 August 2018; Accepted: 17 October 2018; Published: 19 October 2018



**Abstract:** A centrifugal compressor working with supercritical CO<sub>2</sub> (S-CO<sub>2</sub>) has several advantages over other supercritical and conventional compressors. S-CO<sub>2</sub> is as dense as the liquid CO<sub>2</sub> and becomes difficult to compress. Thus, during the operation, the S-CO<sub>2</sub> centrifugal compressor requires lesser compression work than the gaseous CO<sub>2</sub>. The performance of S-CO<sub>2</sub> compressors is highly varying with tip clearance and vanes in the diffuser. To improve the performance of the S-CO<sub>2</sub> centrifugal compressor, knowledge about the influence of individual components on the performance characteristics is necessary. This present study considers an S-CO<sub>2</sub> compressor designed with traditional engineering design tools based on ideal gas behaviour and tested by SANDIA national laboratory. Three-dimensional, steady, viscous flow through the S-CO<sub>2</sub> compressor was analysed with computational fluid dynamics solver based on the finite volume method. Navier-Stokes equations are solved with K- $\omega$  (SST) turbulence model at operating conditions in the supercritical regime. Performance of the impeller, the main component of the centrifugal compressor is compared with the impeller with vaneless diffuser and vaned diffuser configurations. The flow characteristics of the shrouded impeller are also studied to analyse the tip-leakage effect.

**Keywords:** supercritical carbon dioxide; centrifugal compressor; real gas effect; tip clearance; diffuser

## 1. Introduction

The CO<sub>2</sub> maintained at the temperature, and pressure higher than its critical point value (31.106 bar and 31.106 K) is known as supercritical carbon dioxide (S-CO<sub>2</sub>). S-CO<sub>2</sub> is neither a gas nor a liquid; it is highly dense fluid as a liquid meanwhile its diffusivity is as high as a gas. S-CO<sub>2</sub> has no surface tension with low viscosity, and hence it effuses through solid like a gas. This unique combination of properties in S-CO<sub>2</sub> is successfully utilized in various engineering applications. For example, superior solvent characteristics were used in pharmaceutical industry, extraction nature in petrochemical refining, non-flammable and non-toxic characteristics in food processing, higher convection rather than diffusivity nature in chemical separation, and textile dyeing [1]. In recent years, due to several reasons such as low toxicity nature and strict environmental regulations, the research interest on S-CO<sub>2</sub> is increasing in both academic and industrial sectors [2–4].

Thermodynamic cycle with S-CO<sub>2</sub> as a working fluid has several advantages than the conventional cycles [5] mainly due to the three following reasons. (1) S-CO<sub>2</sub> has lower compression ratio provides higher compression efficiency; (2) high density of S-CO<sub>2</sub> makes the turbo-machinery size extremely small; (3) the excellent heat transfer and thermodynamic properties favour for high-efficiency heat exchanger [6]. Near the critical point, supercritical carbon dioxide (S-CO<sub>2</sub>) exhibits a sharp variation in thermodynamic properties. For example, the isobaric specific heat capacity attains a peak value near

the critical point and decreases from that peak value in an oscillating manner along the pseudo-critical line as shown in Figure 1a. At the critical temperature and pressure, the density discontinuously raises from  $300 \text{ kg/m}^3$  to  $600 \text{ kg/m}^3$  as shown in Figure 1b. These abrupt variation in the properties near the critical point makes the convergence of numerical simulations a challenging task [7]; the simulation either diverges during initial iterations itself or not at all converges. Irrespective of better design calculations, the materials used, and other conditions, the primary factor going to affect the output of such S-CO<sub>2</sub> turbo-machinery is the thermodynamic properties [8].

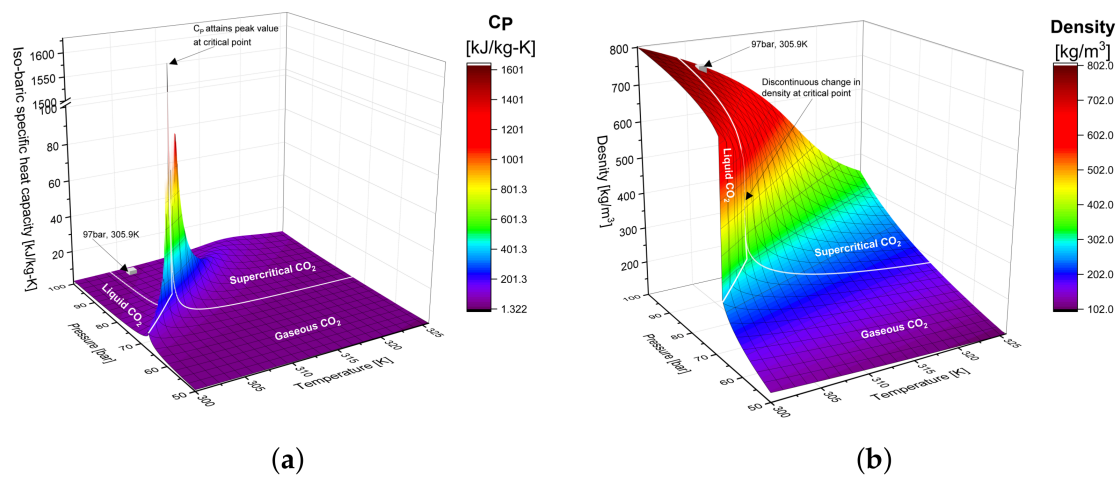


**Figure 1.** Variation of thermodynamic properties near the critical point. (a) Iso-baric specific heat near critical point. (b) Variation of density near critical point.

A significant number of studies are done on the turbo-component effects on centrifugal impeller operating on fluids behaving like an ideal gas [3,9]. However, the studies on the unconventional flow behaviour of supercritical fluids are marginal [10]. In a conventional compressor, the working fluid can be approximated to a fully compressible, whereas in S-CO<sub>2</sub> compressors the non-linear fluid properties are also involved. Therefore, an effective designing and analysis require a real gas equation of state with an accurate prediction of thermodynamic properties of fluids. Baltadejev et al. [11] compared different equation of state and concluded that Span and Wagner equation of state [12] is most suitable for numerical simulation of S-CO<sub>2</sub> compressor.

Centrifugal compressors working with non-ideal fluids are usually designed with tools developed for general gas compressors [13,14], and these non-ideal compressors are subjected to operate at conditions other than design point. The usage of convention design tools in designing of non-ideal compressors affects the performance and to measure its impact; it is necessary to analyse the performance characteristics [15]. Pecnik et al. [16] investigated the laminar flow of S-CO<sub>2</sub> through the impeller configuration without tip clearance and showed that the interpolation of the thermodynamic properties near vapour-liquid-equilibrium region is a better strategy for achieving convergence of the numerical solution. Since the tip clearance is not considered in the numerical model, the calculated pressure ratio was lesser, and the mass flow rate was higher than SANDIA National Laboratories (SNL) results. Inlet pressure close to the critical point shows a high risk of appearance of two-phase flow inside the compressor. Pham et al. [17] stated that for a considerable margin to the saturation dome, choosing an inlet pressure away from critical pressure is a better option than choosing the temperature.

In this present study, performance analysis has been carried out for an S-CO<sub>2</sub> centrifugal compressor designed by SNL [18] with conventional design tools and the surrogate model which mostly approximates the ideal gas behaviour. The insight knowledge of the performance characteristics of the individual components gives a significant advantage for the development and improvement of S-CO<sub>2</sub> compressors. The aerodynamic design of turbo-machinery operating in the supercritical region

depends on these numerical results. Therefore, the design configurations with impeller only, impeller with vaneless diffuser and vaned diffuser are investigated in this present work. Performance of S-CO<sub>2</sub> centrifugal compressor is analysed at a constant inlet thermodynamic state condition and a different mass flow rate. The operating conditions were selected as same as that of design conditions except the inlet pressure is maintained slightly higher to avoid any phase transition.

## 2. Materials and Methods

### 2.1. Real Gas Property Table

The material properties of S-CO<sub>2</sub> are incorporated in the flow solver in the form of real gas properties (rgp) table. The look-up table approach reduces the computational time up to 50% and increases the numerical stability. The rgp table is generated with a FORTRAN subroutine which calculates the thermodynamic properties of CO<sub>2</sub> from the multiparameter equation of state developed by Span and Wagner. The thermodynamic and physical parameters change discontinuously near the critical point which adversely affects the numerical stability and hence the properties are averaged near the phase change region as described in Pecnik et al. [16]. Since the inlet pressure ( $97 \times 10^5$ ) is reasonably higher than the critical pressure, the final results show that the flow is entirely in a supercritical state and hence the error due to the interpolation near the phase change does not affect the final solution. Recently Ameli et al. [19] showed that rgp table with minimum interval of  $0.267 \times 10^5$  Pa and 0.133 K interval is required for accurate numerical results and the same interval is maintained in this present work.

### 2.2. Compressor Geometry and Mesh

An S-CO<sub>2</sub> centrifugal compressor designed and tested by SNL is considered for this present study. The geometrical design specifications of the impeller and the diffuser vanes are tabulated in Tables 1 and 2 respectively.

**Table 1.** Geometry details of the impeller.

Number of main blades	6	Blade thickness at impeller trailing edge	0.762 mm
Number of splitter blades	6	Blade height at impeller leading edge	1.7 mm
Impeller inlet radius at hub	2.537585 mm	Blade angle of the impeller leading edge at hub	17.88°
Impeller inlet radius at shroud	9.372047 mm	Blade angle of the impeller leading edge at mean radius	37.13°
Impeller exit radius	18.68170 mm	Blade angle of the impeller leading edge at shroud	50°
Full blade length	25 mm	Blade angle of the impeller trailing edge	−50°
Splitter blade length	12.5 mm	Angle between streamlines and shaft at impeller inlet	0°
Axial length of the impeller	15.9 mm	Angle between streamlines and shaft at impeller exit	90°
Clearance gap at impeller tip	0.254 mm	Blade thickness at impeller leading edge	0.762 mm

**Table 2.** Geometry details of the vaned diffuser.

Number of vanes	17	Blade height at diffuser exit	1.8 mm
Diffuser inlet radius	18.5 mm	Diffuser channel length	10.6 mm
Diffuser exit radius	26.0 mm	Blade thickness at diffuser inlet	0.0 mm
Blade angle at diffuser inlet	71.5	Blade thickness at diffuser exit	3.35 mm
Blade height at diffuser inlet	1.8 mm		

The Ansys meshing tool, turbogrid is used for grid generation because it provides customised control during grid generation of the centrifugal compressor. Near the wall surfaces such as the hub,

shroud, blade and blade tip, the grid points were densely placed to ensure the  $y^+$  value less than 5. For impeller without tip clearance, cases with different total mesh count such as  $5 \times 10^4$ ,  $1 \times 10^5$ ,  $1.5 \times 10^5$ ,  $2 \times 10^5$ , and  $2.5 \times 10^5$  were simulated for grid independence test as shown in Figure 2. The isentropic efficiency calculated with a model consists of  $2 \times 10^5$  grid cells are not change more than 0.1% than the calculated results of  $2.5 \times 10^5$  case. Hence, the mesh with  $2 \times 10^5$  grid cells is selected for the impeller with zero-tip clearance. Similarly, for impeller with tip clearance, with vaneless diffuser and vaned diffuser numerical models with the total mesh count of  $4 \times 10^5$ ,  $6 \times 10^5$ , and  $9 \times 10^5$  respectively were selected. The grid of different configurations are shown in Figure 3, and their corresponding meridional geometries are represented in inset figure.

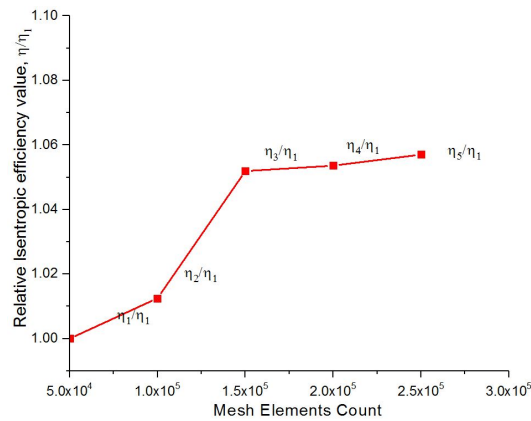


Figure 2. Mesh independence test for impeller without tip clearance configuration.

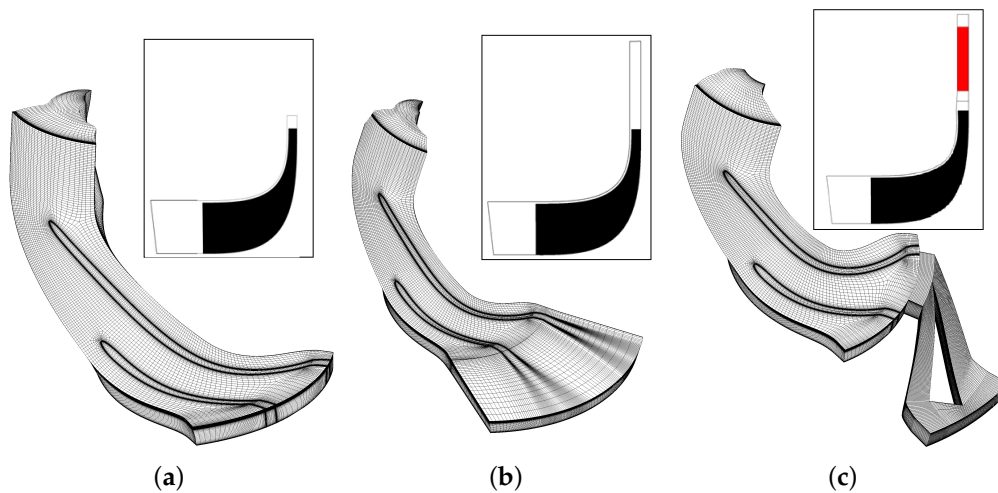


Figure 3. Computational domains for different centrifugal compressor configurations. Inset figures represent the meridional geometry. (a) Impeller alone. (b) Impeller with vaneless diffuser. (c) Impeller with vaned diffuser.

### 2.3. Numerical Methodology

Three-dimensional, steady, viscous, compressible flow through centrifugal compressor was simulated with commercial computational fluid dynamics solver ANSYS CFX V19 which is based on finite volume method. In this present study, the compressible flow is simulated by using the second order discretisation for solving flow variables in the fundamental flow equations expressed in Equations (1)–(3). The variables density, pressure, temperature, total enthalpy, and thermal conductivity

are represented as  $\rho$ ,  $P$ ,  $T$ ,  $h_{tot}$ , and  $\lambda$  respectively. The terms  $\mathbf{U}$  and  $\tau$  represent the velocity vector and viscous stress tensor respectively.

$$\nabla \odot (\rho \mathbf{U}) = 0 \quad (1)$$

$$\nabla \odot (\rho \mathbf{U} \otimes \mathbf{U}) = -\nabla P + \nabla \odot \tau \quad (2)$$

$$\nabla \odot (\rho \mathbf{U} h_{tot}) = \nabla \odot (\lambda \nabla T) + \nabla \odot (\mathbf{U} \odot \tau) \quad (3)$$

The substantial variation in thermodynamic properties near the critical point considerably affects the results based on the selection of the turbulence models. Shear-Stress-Transport (SST) model modification done on original  $k$ - $\omega$  turbulence model is considered as suitable turbulence model for the simulation of S-CO<sub>2</sub> flow in the earlier studies [3,11,19]. Hence, the turbulence parameters were obtained with consideration of  $K$ - $\omega$  (SST) turbulent model which is implicitly resolved along with the fundamental equations.

A single flow passage with the main blade and a splitter blade is modelled to reduce the computational cost, and the geometry simplification is done by using the rotational periodicity boundary condition as shown in Figure 4. The rotational speed of the centrifugal compressor is set as 50,000 rpm which corresponds to the shaft speed in a test loop in SNL [15]. At design point, SNL compressor has inlet pressure of 76.9 bar and 305.3 K with a mass flow rate of 3.53 kg/s. The compressor needs to operate at substantially different inlet conditions other than the design point. Hence, the inlet pressure and temperature is set as  $97 \times 10^5$  Pa and 305.9 K respectively as in the Ref. [15] to avoid any phase change (marked as a cube symbol in Figure 1a,b). A turbulence intensity of 5% is assumed at the inlet. The boundary condition at the outlet is set as mass flow rate, and the compressor performance is calculated by varying the mass flow rate. All the wall surfaces are provided with no slip and adiabatic boundary conditions. Single rotating reference frame and multiple rotating reference frame is considered for the numerical models of the impeller without diffuser and impeller with diffuser respectively. In the impeller zone, the blade and the hub were considered as a rotating wall. For the unshrouded impeller configuration, the shroud also considered as rotating wall while the tip clearance configuration, it is imposed with counter-rotating wall boundary condition. The frozen interface was assumed between the impeller zone and diffuser zone interface.

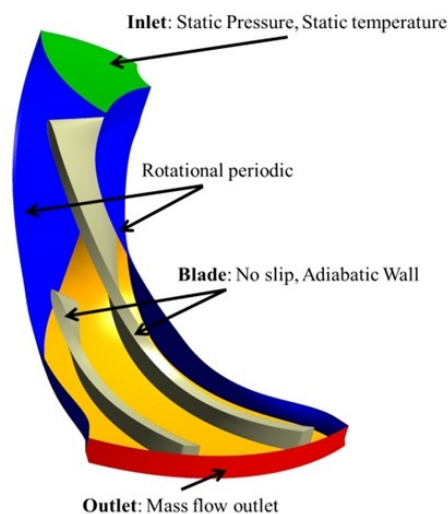


**Figure 4.** Boundary conditions used for the computational model of impeller alone configuration.

Initially, a temporary solution is obtained using  $K$ - $\epsilon$  turbulence model with a coarser mesh having  $y^+$  values of 30 to 300 and with a coarser rgp table of with an interval of 0.5 K and  $0.5 \times 10^5$  Pa. Later, the numerical model with finer grid was simulated using  $K$ - $\omega$  (SST) turbulence model after initialising from the earlier obtained temporary solution. Solutions were considered as converged after

the residuals of flow and turbulence parameters fall below  $10^{-4}$  with the isentropic efficiency, and total pressure ratio are not changed more than 0.01% and 0.005% respectively from the values of the earlier iteration.

### 3. Validation

For the validation of the present numerical methodology, the simulated results were compared with the experimental results measured at SNL with an inlet temperature of 309 K and pressure of  $92 \times 10^5$  Pa [15]. Figure 5 shows the comparison of the experimental isentropic efficiency and the computational results of the impeller with vaned configuration. The calculated total-static isentropic efficiency shows a good agreement with the experimental data of SNL. However, an appreciable difference is recognized at the lower flow coefficients which can be attributed to the undefined position of experimental inlet conditions in the SNL report. Since the thermodynamic state of inlet condition is closer to the pseudo-critical line, a small change in inlet temperature or pressure produces large exit properties. Figure 6 represents the results of  $y^+$  contour on the hub and wall surface with K- $\omega$  (SST) turbulence model. The  $y^+$  values are close to unity on blade surfaces except at the trailing edge. Even though a maximum value  $y^+$  of 4.3 exists on the corner of blade trailing edge, this grid point still lies in the viscous sub-layer.

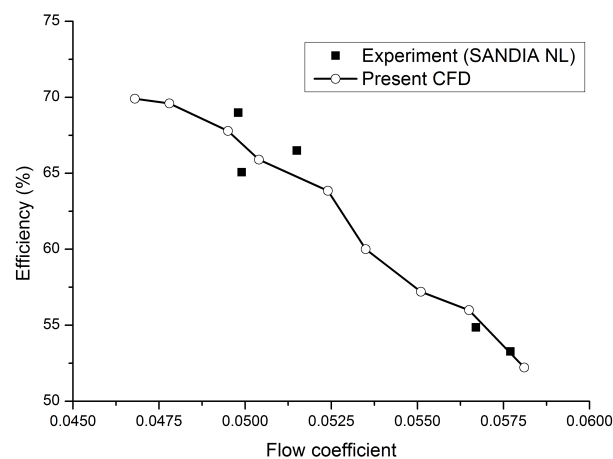


**Figure 5.** Comparison of present numerical results with the SNL experimental results [15] at inlet temperature of 309 K and pressure of  $92 \times 10^5$  Pa.

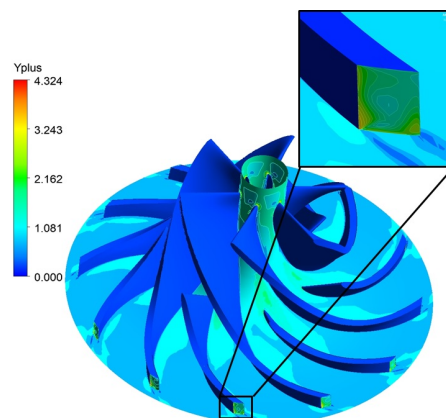


**Figure 6.** The  $y^+$  contour on hub and blade surface with K- $\omega$  turbulence model. The blade trailing edge region is zoomed in the inset figure to show the maximum  $y^+$  value.

### 4. Results and Discussion

The performance map of different configurations such as impeller alone, impeller with vaneless diffuser and impeller with vaned diffuser were analysed at a constant inlet pressure and temperature with varying mass flow rate, and the results were presented in this section.

#### 4.1. Effect of Tip Clearance

Performance characteristics of the impeller without and with tip clearance configurations for the impeller without and with tip clearance configurations are shown in Figure 7. The isentropic efficiency ( $\eta_{iso}$ ) defines the ratio between stagnation enthalpy ( $H$ ) rise of an isentropic compression process to that of a real compression process and is expressed in Equation (4). In this equation, the subscripts “in” and “out” denotes the inlet and outlet section respectively while the subscript “iso” indicates the value when the compression takes place at constant entropy. Tip clearance reduces the value of “ $H_{out}$ ” as in Figure 7, and hence, its “ $\eta_{iso}$ ” value is always lower than impeller with zero-tip clearance configuration. The difference between the “ $\eta_{iso}$ ” values of two configurations increases from 9% at 3 kg/s to 12% at 4.75 kg/s; this indicates the increase in loss due to tip-leakage flow with the increasing mass flow rate.

$$\eta_{iso} = \frac{H_{out,iso} - H_{in}}{H_{out} - H_{in}} \tag{4}$$

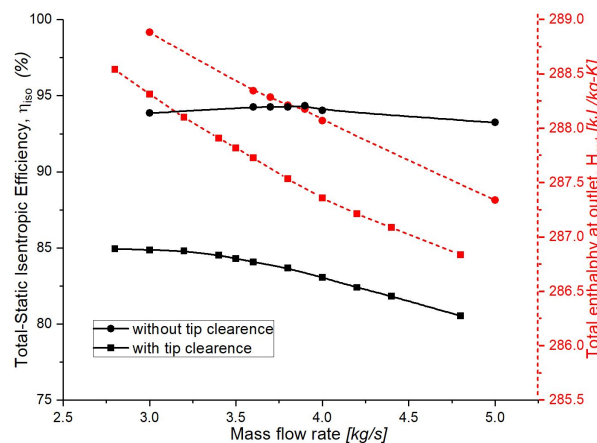


**Figure 7.** The isentropic compression efficiency and the total enthalpy at outlet for the impeller without and with tip clearance configurations. Solid lines indicate the total-static isentropic efficiency and the dashed lines shows the total enthalpy at the outlet.

In the tip clearance configuration, the pressure at outlet get severely reduced as shown in Figure 8b than the zero-tip clearance configuration as in Figure 8a. Along the circumferential direction, the pressure distribution is found with high gradient for zero-tip clearance configuration, while the pressure is more evenly distributed for the tip clearance configuration. The presence of tip gap induces secondary flows which allow the mixing of the flows from the pressure side to the suction side which results in an evenly distributed pressure. Additionally, this mixing causes high windage losses and reduces efficiency.

The Figure 9 shows blade pressure loading at the constant span of 10%, 50% and 90% from the hub for the without and with tip clearance configurations at a mass flow rate of 4 kg/s. The data is normalized to 0 to 1 from the leading edge to trailing edge of the main blade. Up to the normalized streamwise position of 0.5, the pressure distribution of the main blade is nearly the same for both the configurations. After the normalized streamwise position of 0.5, the pressure starts to deteriorate in the tip clearance configuration due to tip leakage. The presence of tip clearance equally affects the

flow behaviour at midspan and near hub region, but profoundly influence the flow near the shroud. Since a constant gap exists between the shroud and blade tip, blade section near the trailing edge lies below the 90% span. This results in truncation in the blade pressure loading profile near shroud at the normalized streamwise position of 0.73. Near shroud, the mixing between primary and secondary flow is higher and hence the pressure rise stalls in both main blade and splitter blade.

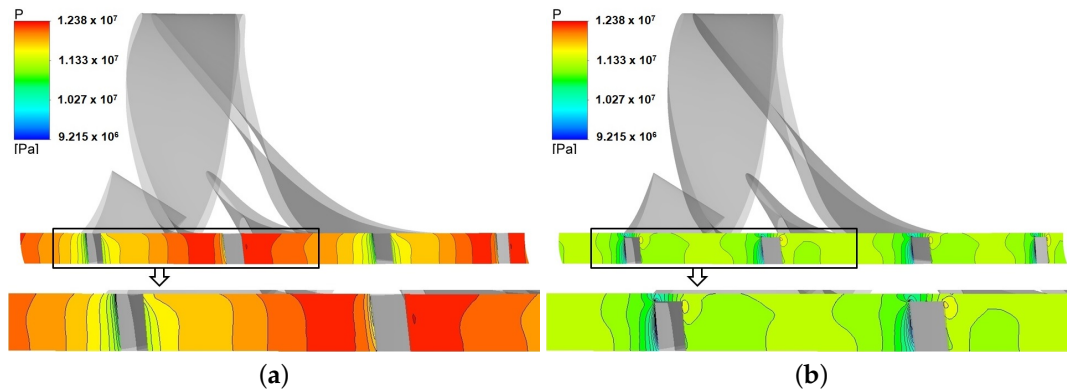


**Figure 8.** Circumferential pressure contour at the trailing edge for mass flow rate of 4 kg/s. (a) Impeller alone. (b) Impeller with vaneless.

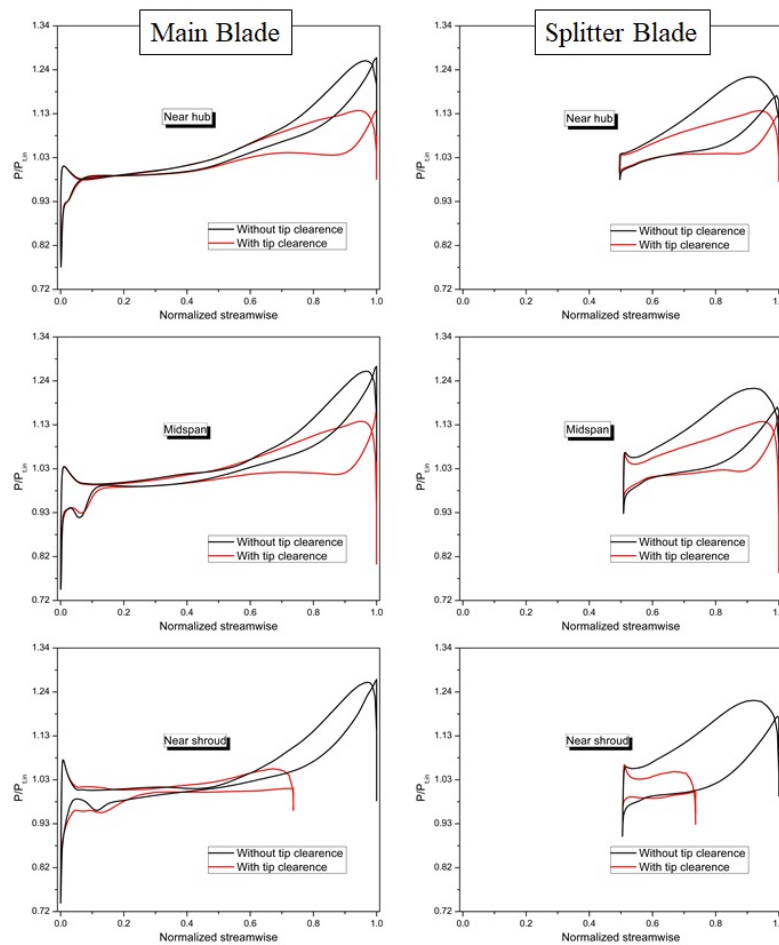


**Figure 9.** Blade pressure loading for impeller without tip clearance and with tip clearance at a mass flow rate of 4 kg/s.

The entropy generation includes all the losses occurring in the flow passage, and the higher entropy generation denotes a lower efficiency. For the zero-tip clearance configuration, the maximum entropy generation is 1263 J/kg K as seen in Figure 10a while the maximum entropy value rises to 1267.7 J/kg K on the inclusion of tip clearance as seen in Figure 10b. Since the walls are imposed with the adiabatic boundary condition, the only source of entropy generation is flow irreversibility. In the unshrouded compressor, the shroud is stationary, and hence the low momentum flow near the shroud does not overcome the pressure gradient in the radial direction which results in a re-circulation region and a higher entropy generation. In a shrouded compressor, the shroud is rotating at same rotational speed as the blade, and the low momentum flow is absent which results in a uniform flow at the outlet. The losses in zero-tip clearance configuration are the sum of minor losses due to friction, the kinetic energy dissipation and the shear work. Therefore, the entropy generation is steady in streamwise direction without any gradient. In tip clearance configuration, in addition to these losses, the mixing loss happens due to tip clearance flow which causes the sudden increment of entropy generation.

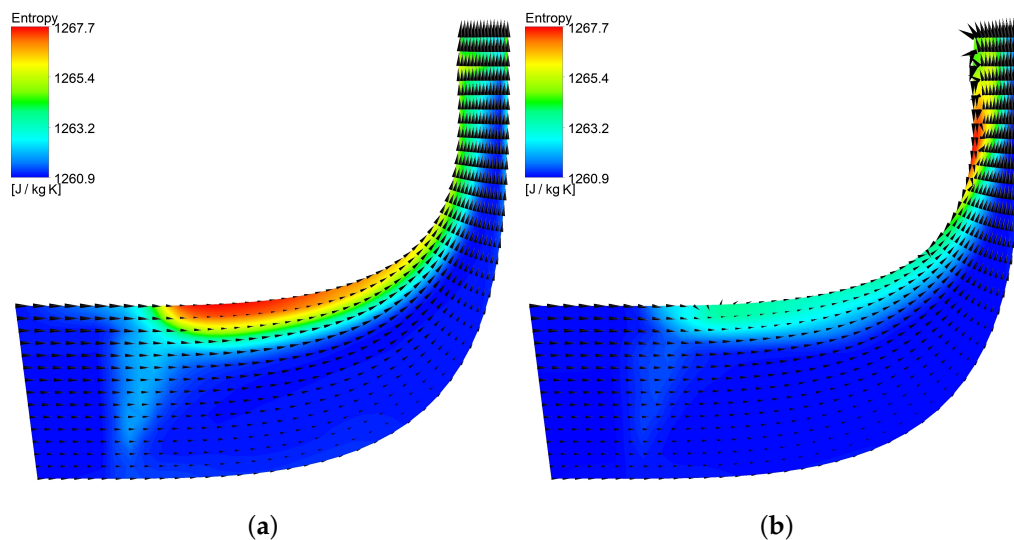


**Figure 10.** Velocity vector plot on the meridional plane with mass flow rate averaged entropy at a mass flow rate of 4 kg/s. The flow at the outlet section is uniform in impeller without tip clearance configuration, while it becomes a wake flow in with tip clearance configuration. (a) Impeller without tip clearance. (b) Impeller with tip clearance.

#### 4.2. Effect of Diffuser

The inclusion of diffuser on the impeller with tip clearance configuration (hereafter called as impeller alone configuration) increases the efficiency as shown in Figure 11. The efficiency of vaneless configuration is higher than the vaned and impeller alone configurations. At the lower mass flow rates, the pressure ratio of the vaned diffuser is higher than the vaneless and impeller alone configurations. Despite this high-pressure rise of the vaned diffuser, its efficiency already begins to drop in these low mass flow rate range. On further increment in mass flow rate, the pressure ratio of vaned diffuser drops at a higher rate (nearly twice) than the vaneless diffuser. The impeller alone configurations surge at the mass flow rate of 2.75 kg/s and this limit shift to the left on the inclusion of diffuser. The vaneless diffuser has a broader range of operational mass flow rate than the vaned diffuser which is analogous to the conventional compressor. In the conventional compressor, at an inlet pressure slightly higher than design point, the vaned diffuser accomplishes a better performance than the vaneless diffuser. In this present case of S-CO<sub>2</sub> compressor designed with conventional design tools developed with ideal gas behaviour, the performance of the vaned diffuser is much lower than the vaneless diffuser despite the mass flow rate and inlet temperature is same as the design point. This result indicates the

necessity for consideration of real gas effects during the design process and development of design tools, especially for S-CO<sub>2</sub> compressor.

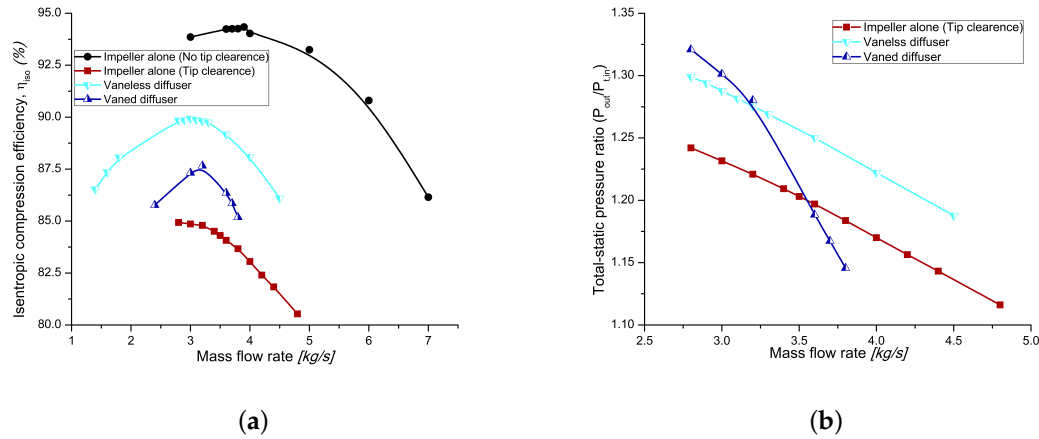


**Figure 11.** Performance characteristics of various configurations. (a) Comparison of isentropic compression efficiency of different configurations. The efficiency increases on the inclusion of the diffuser section in the impeller with the tip clearance configuration and attains a peak value near the design mass flow rate of 3.53 kg/s. (b) Comparison of the total-static pressure ratio of different configurations. The pressure ratio for vaned diffuser decreases at a higher rate than the vaneless diffuser configuration which indicates the vaned diffuser becomes less efficient at mass flow rate more than 3.25 kg/s.

The region with lower Mach number is formed in front of the leading edge of splitter blade due to flow blockage, and this region is bigger in the vaned diffuser than the vaneless diffuser as shown in Figure 12. This larger low-Mach region in vaned diffuser indicates the higher flow blockage, and hence the performance characteristics degenerate at lower mass flow rate than vaneless configuration. The low-Mach region near the trailing edge is also the reduced with the vaneless diffuser. Thus, the vaneless diffuser reduces the blockage effect arises due to the tip clearance than the vaned diffuser configuration.

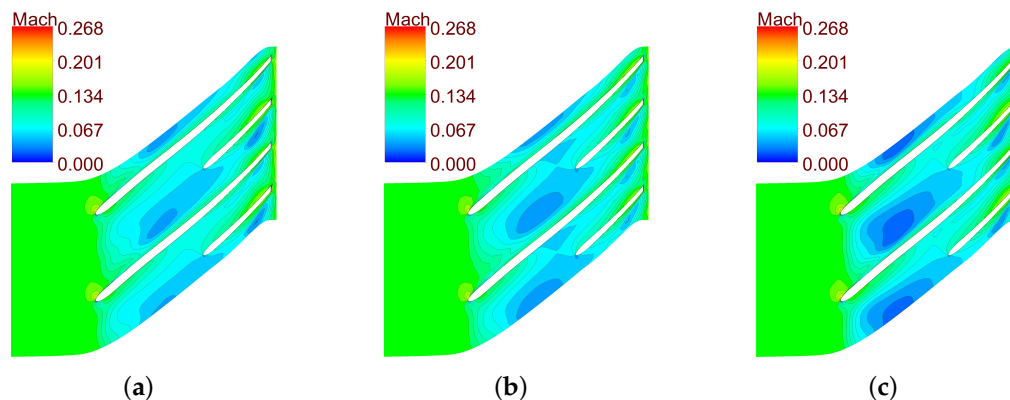


**Figure 12.** Relative Mach number contour plot at the span of 80% from hub to shroud at a mass flow rate of 3.2 kg/s. (a) Impeller alone. (b) Impeller with vaneless. (c) Impeller with vaned.

Near the leading edge, flow approaches at a higher angle of incidence which causes more acceleration on the suction side as shown in Figure 13 and due to this expansion, the Mach number

increases suddenly. The high Mach number region near leading edge is relatively stronger in the vaned diffuser while the vaneless diffuser weakens. This sudden acceleration near the leading edge of the main blade causes the pressure to decrease locally, and pressure decreases lower than inlet pressure in some regions as shown in Figure 14. On operating S-CO<sub>2</sub> compressor with inlet pressure closure to the critical point, pressure may drop below the critical pressure, and a phase transition may occur, the single phase flow eventually no longer existed. The tip leakage flow causes secondary flow which also induces the formation of a similar region with lower pressure the inlet condition on the blade tip in Figures 14a,c. For vaneless diffuser case in Figure 14b, it can be seen that the lower pressure region on the tip of main blade vanishes. Further, the region with a pressure lower than inlet pressure exists even at the trailing edge of both main blade and splitter blade, thus demonstrates the severe risk of formation of two-phase flow as in Figure 15. The absence of lower pressure region on the splitter blade tip of vanless diffuser configuration shows that it reduces the risk of phase transition on operating near critical point.

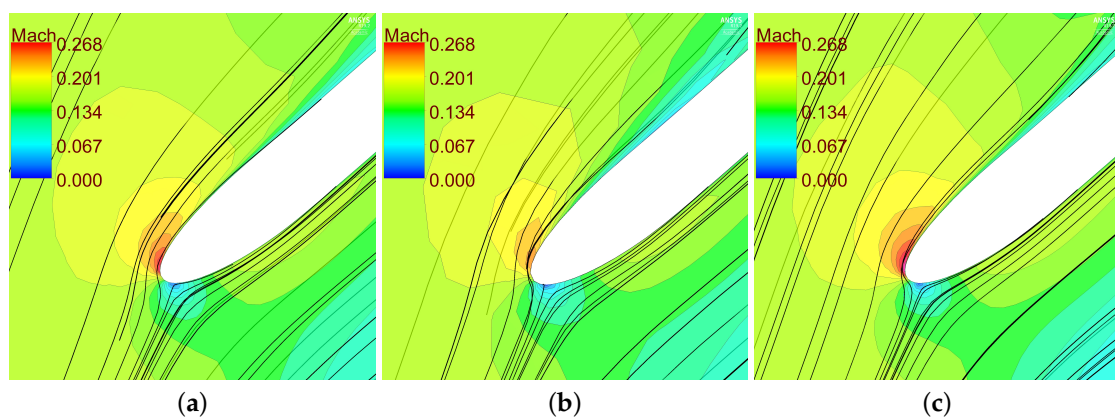


**Figure 13.** Streamlines near leading edge of the main blade on the relative Mach number contour at a mass flow rate of 3.2 kg/s. (a) Impeller alone. (b) Impeller with vaneless diffuser. (c) Impeller with vaned diffuser.

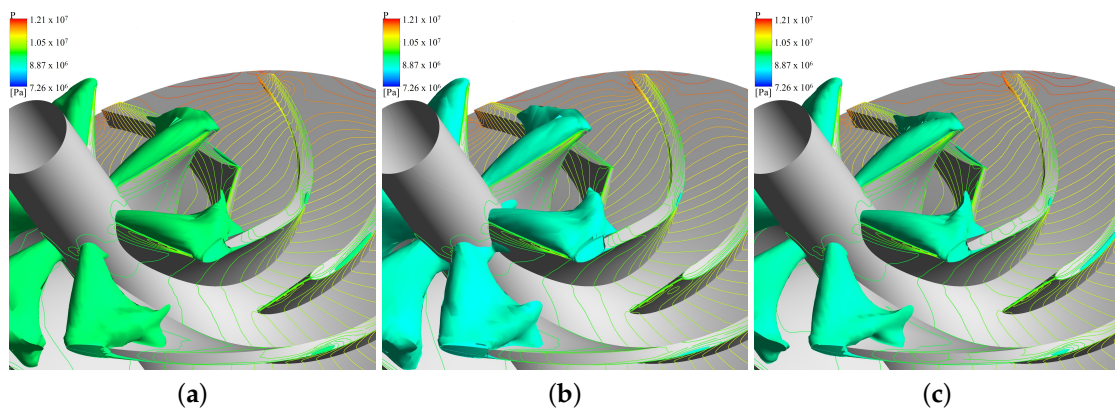


**Figure 14.** Volume near leading edge shows the regions where the pressure is lower than the inlet pressure at mass flow rate of 3.2 kg/s. (a) Impeller alone. (b) With vaneless diffuser. (c) With vaned diffuser.

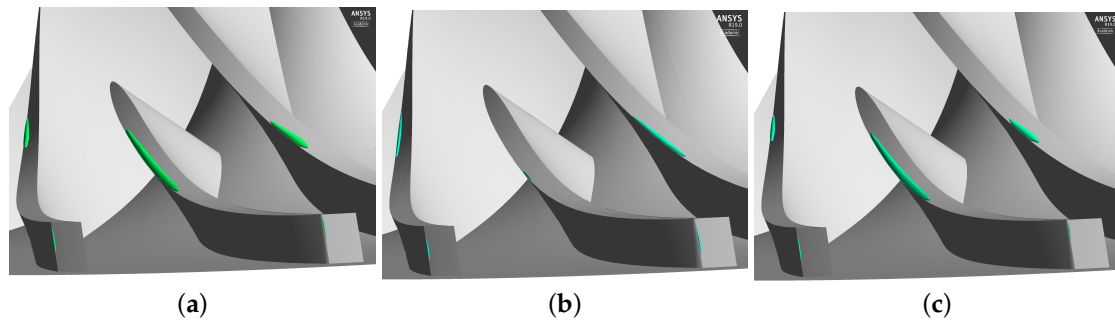


**Figure 15.** Volume shows the regions near trailing edge where the pressure is lower than the inlet pressure at a mass flow rate of 3.2 kg/s. (a) Impeller alone. (b) With vaneless diffuser. (c) With vaned diffuser.

The influences of different turbo-machinery components on the temperature and entropy at the outlet in a different manner as shown in Figure 16. Even though, the entropy at the outlet of impeller alone is much lower than the two other cases; the lower efficiency in impeller alone is due to change in specific heat capacity. As in Equation (4), the isentropic compression efficiency is a function of outlet enthalpy which is a product of isobaric specific heat capacity and temperature. For a slight change in a thermodynamic state near pseudo-critical line, the specific heat capacity value changes abruptly due to real gas effect as shown in Figure 1a. This abrupt variation in the value of specific heat capacity affects the “ $H_{out}$ ” value which in turn affects the efficiency.

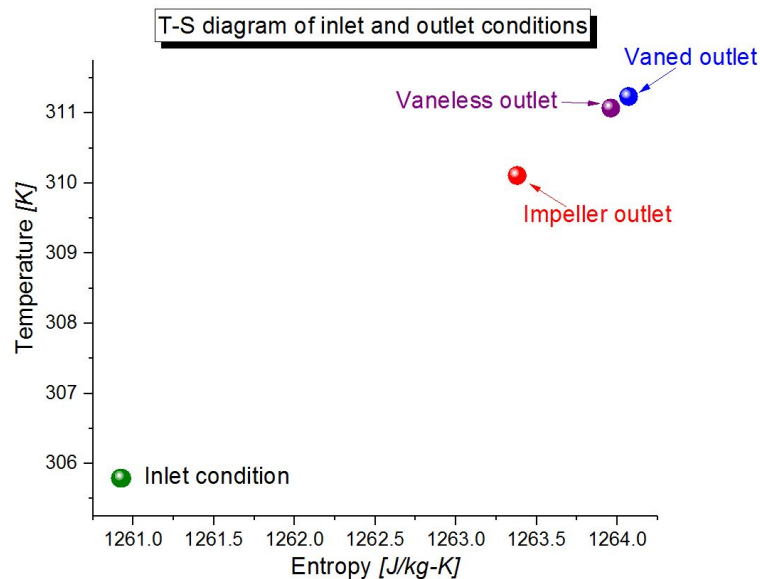


**Figure 16.** T-S diagram shows the inlet and outlet condition at the mass flow rate of 3.2 kg/s.

#### 4.3. Flow Field Near the Impeller and Diffuser Interface

At a lower mass flow rate of 1.4 kg/s, the flow approaches the leading edge of diffuser vane blade at higher flow angle as shown in Figure 17a. Hence, a re-circulation region forms near the leading edge of diffuser vane blade which generates the entropy and the efficiency of vaned configuration drops at a lower mass flow rate. At a higher mass flow rate of 3.8 kg/s, flow approaches the leading edge of vane blade at lower incidence angle as shown in Figure 17b. Again a re-circulation region forms but at the other side of vane blade, and this causes a decline in performance at a higher mass flow rate as in Figure 11. For constant diffuser width, the flow angle is a function of fluid density which changes

abruptly in the non-ideal like S-CO<sub>2</sub>. The flow incidence angle changes for a small variation in mass flow rate in S-CO<sub>2</sub> compressor which limits the operating range of vaned diffuser.

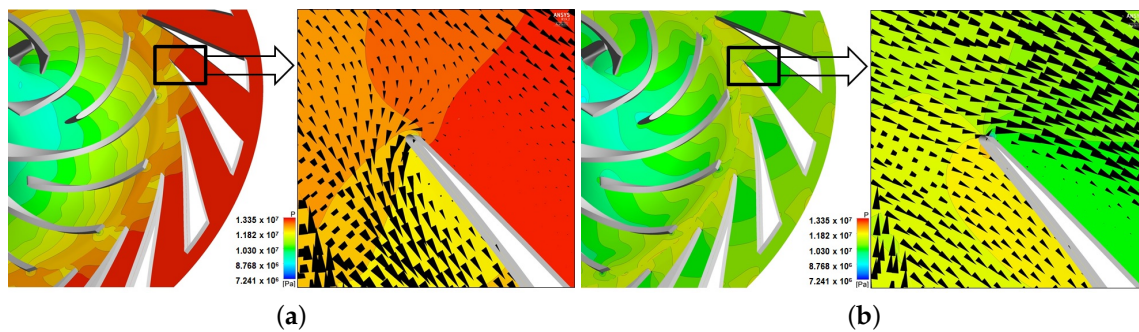


**Figure 17.** Pressure contour and velocity vector at span 50% span for impeller alone with vaned diffuser configuration. (a) Impeller with vaned diffuser at mass flow rate of 1.4 kg/s. (b) Impeller with vaned diffuser at mass flow rate of 3.8 kg/s.

The peak pressure which is represented as the maximum pressure value in the pressure contour is an indication of pressure rise. The pressure attains a maximum value for lower mass flow rate, and the peak pressure decreases as the mass flow rate increases as shown in the pressure contour of the vaneless diffuser configuration as shown in Figure 18. The flow becomes more distorted in the circumferential direction with increasing mass flow rate as seen in Figure 18c. As seen in the velocity vector of flow field for the vaneless diffuser configuration in Figure 19, the flow angle changes from the logarithmic spiral direction to an outward straightened flow in the diffuser section with increasing mass flow rate. For optimum performance, the flow angle direction is similar to that of the mass flow rate of 2.9 kg/s. The absence of diffuser vanes allows the vaneless diffuser in S-CO<sub>2</sub> compressor to operate at a broader range of mass flow rate with better performance.

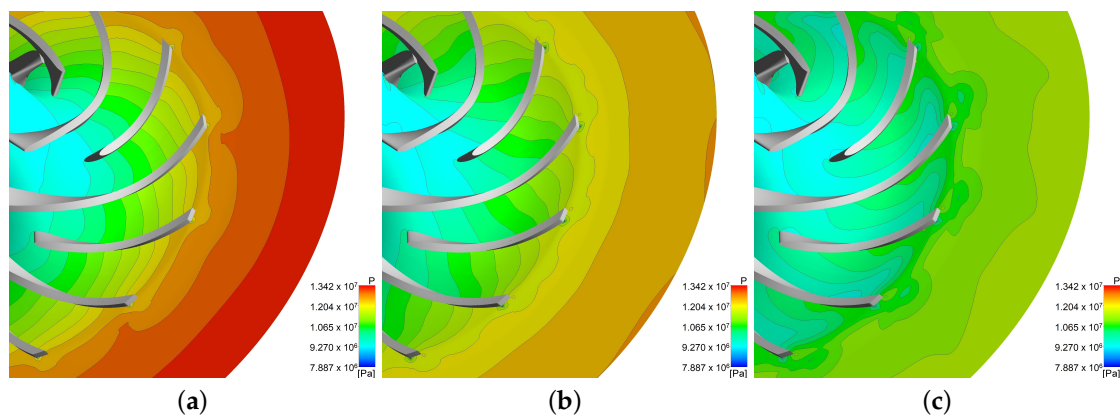


**Figure 18.** Pressure contour at span 50% span of impeller with vaneless diffuser. (a) Vaneless diffuser at mass flow rate of 1.4 kg/s. (b) Vaneless diffuser at mass flow rate of 2.9 kg/s. (c) Vaneless diffuser at mass flow rate of 4.5 kg/s

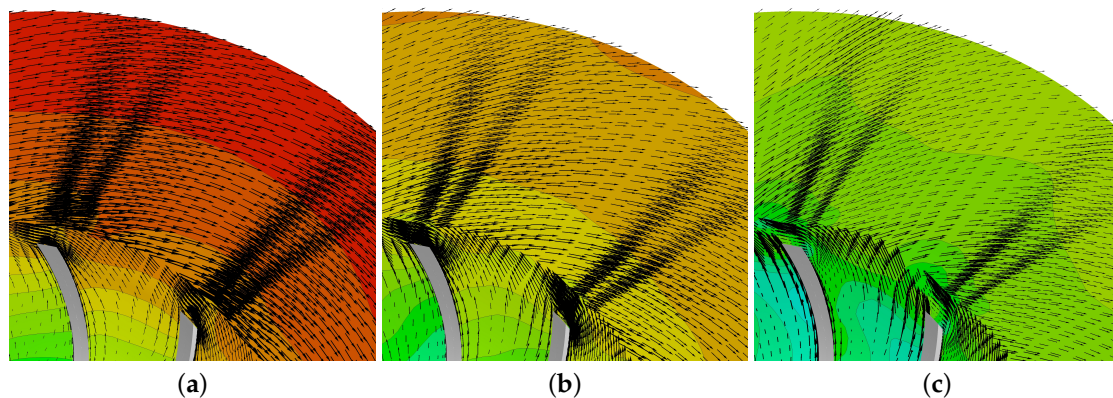


**Figure 19.** Velocity vectors near trailing edge of the main blade for vaneless configuration. (a) Vaneless diffuser at mass flow rate of 1.4 kg/s. (b) Vaneless diffuser at mass flow rate of 2.9 kg/s. (c) Vaneless diffuser at mass flow rate of 4.5 kg/s.

## 5. Conclusions

The S-CO<sub>2</sub> centrifugal compressor designed with traditional engineering tools and implemented in the test loop of SANDIA national laboratories is considered for this study. Numerical results are compared with the experimental results, and a good agreement was found which validates the present numerical methodology. To investigate the effects of turbo-machinery components on performance, impeller without tip clearance, with tip clearance, impeller with vaneless diffuser and with vaned diffuser configurations were simulated with constant inlet conditions and at varying mass flow rate.

Due to the high density of S-CO<sub>2</sub>, the windage losses in tip clearance configuration is higher and highly degrade the performance of the tip clearance configuration. Tip clearance decreases the pressure rise and also reduces the isentropic compression efficiency. Uniform flow pattern at the outlet of the without tip clearance configuration changes into wake flow on the inclusion of small tip clearance. At mass flow rate more than design point, the vaned diffuser increases the low-Mach region before the splitter blade due to flow blockage effect while the vaneless reduces this region. Thus, the vaneless diffuser configuration reduces the flow blockage effect caused by tip leakage and improves the performance characteristics of impeller alone configuration. On operating the S-CO<sub>2</sub> compressor near the critical point, the risk of phase transition is severe. The vaneless diffuser configuration decreases the risk of the pressure lowering below the inlet condition and hence reduces the phase transition risk.

The approximation based on the ideal gas behaviour in the design of non-ideal compressor severely affects the performance for a slight change in design point inlet pressure despite the mass flow rate and inlet temperature are maintained as same as design point condition. Hence, it is necessary to develop methodologies, empirical relations and engineering design tools by incorporating the non-ideal gas properties for a broader range of operation.

**Author Contributions:** All the authors have contributed substantially to the publication.

**Funding:** This work was supported by a Research Grant of Andong National University.

**Conflicts of Interest:** The authors declare no conflict of interest.

## References

1. Cabeza, L.F.; de Gracia, A.; Fernández, A.I.; Farid, M.M. Supercritical CO<sub>2</sub> as heat transfer fluid: A review. *Appl. Therm. Eng.* **2017**, *125*, 799–810. [[CrossRef](#)]
2. Ayub, Z. Recent developments in CO<sub>2</sub> heat transfer. *Heat Transf. Eng.* **2005**, *26*, 3–6. [[CrossRef](#)]

3. Fan, X.; Wang, Y.; Zhou, Y.; Chen, J.; Huang, Y.; Wang, J. Experimental study of supercritical CO<sub>2</sub> leakage behavior from pressurized vessels. *Energy* **2018**, *150*, 342–350. [[CrossRef](#)]
4. Tokanai, H.; Ohtomo, Y.; Horiguchi, H.; Harada, E.; Kuriyama, M. Heat transfer of supercritical CO<sub>2</sub> flow in natural convection circulation system. *Heat Transf. Eng.* **2010**, *31*, 750–756. [[CrossRef](#)]
5. Shu, G.; Shi, L.; Tian, H.; Chang, L. Comparison and Selection Research of CO<sub>2</sub>-Based Transcritical Rankine Cycle Using for Gasoline and Diesel Engine's Waste Heat Recovery. *Heat Transf. Eng.* **2017**, *7632*, 1–15. [[CrossRef](#)]
6. Ma, Y.; Liu, Z.; Tian, H. A review of transcritical carbon dioxide heat pump and refrigeration cycles. *Energy* **2013**, *55*, 156–172. [[CrossRef](#)]
7. Lee, J.; Baik, S.; Cho, S.K.; Cha, J.E.; Lee, J.I. Issues in performance measurement of CO<sub>2</sub> compressor near the critical point. *Appl. Therm. Eng.* **2016**, *94*, 111–121. [[CrossRef](#)]
8. Assael, M.J. The importance of thermophysical properties in optimum design and energy saving. In *Energy and Environment*; Mori, Y.H., Ohnishi, K., Eds.; Springer: Tokyo, Japan, 2001; pp. 162–178.
9. Hosseini, M.; Sun, Z.; He, X.; Zheng, X. Effects of Radial Gap Ratio between Impeller and Vaned Diffuser on Performance of Centrifugal Compressors. *Appl. Sci.* **2017**, *7*, 728. [[CrossRef](#)]
10. Wang, Y.; Shi, D.; Zhang, D.; Xie, Y. Investigation on Unsteady Flow Characteristics of a SCO<sub>2</sub> Centrifugal Compressor. *Appl. Sci.* **2017**, *7*, 310. [[CrossRef](#)]
11. Baltadjiev, N.D.; Lettieri, C.; Spakovszky, Z.S. An Investigation of Real Gas Effects in Supercritical CO<sub>2</sub> Centrifugal Compressors. *J. Turbomach.* **2015**, *137*, 091003. [[CrossRef](#)]
12. Span, R.; Wagner, W. A new equation of state for carbon dioxide covering the fluid region from the triple-point temperature to 1100 K at pressures up to 800 MPa. *J. Phys. Chem. Ref. Data* **1996**, *25*, 1509–1596. [[CrossRef](#)]
13. Li, P.Y.; Gu, C.W.; Song, Y. A New Optimization Method for Centrifugal Compressors Based on 1D Calculations and Analyses. *Energies* **2015**, *8*, 4317–4334. [[CrossRef](#)]
14. Liu, Z.; Luo, W.; Zhao, Q.; Zhao, W.; Xu, J. Preliminary Design and Model Assessment of a Supercritical CO<sub>2</sub> Compressor. *Appl. Sci.* **2018**, *8*, 595. [[CrossRef](#)]
15. Fuller, R.L.; Eisemann, K. Centrifugal Compressor Off-Design Performance for Super-Critical CO<sub>2</sub>. In Proceedings of the Supercritical CO<sub>2</sub> Power Cycle Symposium, Boulder, CO, USA, 24–25 May 2011; pp. 1–20.
16. Pecnik, R.; Rinaldi, E.; Colonna, P. Computational Fluid Dynamics of a Radial Compressor Operating with Supercritical CO<sub>2</sub>. *J. Eng. Gas Turbines Power* **2012**, *134*, 122301. [[CrossRef](#)]
17. Pham, H.S.; Alpy, N.; Ferrasse, J.H.; Boutin, O.; Tothill, M.; Quenaut, J.; Gastaldi, O.; Cadiou, T.; Saez, M. An approach for establishing the performance maps of the sc-CO<sub>2</sub> compressor: Development and qualification by means of CFD simulations. *Int. J. Heat Fluid Flow* **2016**, *61*, 379–394. [[CrossRef](#)]
18. Wright, S.A.; Radel, R.F.; Vernon, M.E.; Rochau, G.E.; Pickard, P.S. *Operation and Analysis of a Supercritical CO<sub>2</sub> Brayton Cycle*; SANDIA Report SAND 2010-0171; Sandia National Laboratories: Livermore, CA, USA, 2010; p. 101.
19. Ameli, A.; Afzalifar, A.; Turunen-Saaresti, T.; Backman, J. Effects of Real Gas Model Accuracy and Operating Conditions on Supercritical CO<sub>2</sub> Compressor Performance and Flow Field. *J. Eng. Gas Turbines Power* **2018**, *140*, 062603. [[CrossRef](#)]

